

Digital Twin–Based Beamforming for Interference Mitigation in AF Relay MIMO Systems

Alexander Bonora, Anna V. Guglielmi, Davide Scazzoli, Marco Giordani, *Senior Member, IEEE*,
Maurizio Magarini, Vineeth Teeda, Stefano Tomasin, *Senior Member, IEEE*

Abstract—Beamforming in multiple-input multiple-output (MIMO) systems should take interference mitigation into account. However, for beam form design, accurate channel state information (CSI) is needed, which is often difficult to obtain due to channel variability, feedback overhead, or hardware constraints. For example, amplify-and-forward (AF) relays passively forward signals without measurement, precluding full CSI acquisition to and from the relay. To address these issues, this paper introduces a novel prediction-assisted optimization (PAO) framework for beam form design in AF relay-assisted multiuser MIMO systems. The proposed solution in the AF relay aims at maximizing the signal-plus-interference-to-noise ratio (SINR). Unlike other methods, PAO relies solely on received power measurements, making it suitable for scenarios where CSI is unreliable or unavailable. PAO consists of two stages: a supervised-learning-based neural network (NN) that predicts the positions of transmitters using signal observations, and an optimization algorithm, guided by a digital twin (DT), that iteratively refines the beam direction of the relay in a simulated radio environment. As a key contribution, we validate the proposed framework using realistic measurements collected on a custom-built experimental millimeter wave (mmWave) platform, which enables training of the NN model under practical wireless conditions. The estimated information is then used to update the digital twin with knowledge of the surrounding environment, enabling online optimization. Numerical results show the trade-off between localization accuracy and beamforming performance, and confirm that PAO maintains robustness even in the presence of localization errors while reducing the need for real-world measurements.

Index Terms—Amplify-and-Forward (AF) Relay, Beamforming, Digital Twin, Interference, Neural Network.

I. INTRODUCTION

Dense deployments, multi-user access, and dynamic channel conditions inevitably introduce non-orthogonality into the network, giving rise to interference that can be both severe and unpredictable. To maintain reliable performance, it becomes essential to develop effective interference management techniques tailored to these dynamic environments.

A. Bonora, A. V. Guglielmi, M. Giordani, and S. Tomasin are with the Department of Information Engineering, University of Padova, Padova, Italy. (Corresponding author: A. Bonora, E-mail: alexander.bonora@phd.unipd.it). D. Scazzoli, M. Magarini, and V. Teeda are with the Department of Electronics, Information and Bioengineering, Politecnico di Milano, Milan, Italy. This work was partially supported by the European Commission through the European Union’s Horizon Europe Research and Innovation Programme under the Marie Skłodowska-Curie-SE, Grant Agreement No. 101129618. This work was partially supported by the European Union under the Italian National Recovery and Resilience Plan (NRRP) Mission 4, Component 2, Investment 1.3, CUP C93C22005250001, partnership on “Telecommunications of the Future” (PE00000001 - program “RESTART”)

Most existing beamforming techniques in multiple-input multiple-output (MIMO) systems have been designed to maximize the beamforming gain toward a target user or direction [1]–[3]. Especially when operating in the millimeter wave (mmWave) band, techniques such as discrete Fourier transform (DFT)-based codebooks, hierarchical codebooks, and beam sweeping protocols have been extensively investigated to enhance signal strength while maintaining affordable complexity. These methods have been integrated into wireless standards, including IEEE 802.11ad and 3GPP New Radio (NR), highlighting their practical relevance [4], [5].

However, a key limitation of these approaches is their interference-unaware nature. Specifically, by focusing uniquely on maximizing the desired signal, they neglect the spatial characteristics of potential interfering transmitters, leading to significant performance degradation especially in dense network deployments where multiple links coexist [6], [7]. Indeed, as the density of networks increases (with the proliferation of small cells, relays, and user devices), the ability to mitigate interference becomes critical to sustain high quality of service (QoS). This challenge has motivated the investigation of interference-aware beamforming strategies, such as coordinated beamforming and interference alignment, which explicitly account for multi-user interference in the beam design [8], [9]. Recently, in [10] the authors proposed a decentralized interference-aware codebook learning algorithm for multi-cell MIMO systems that operates without inter-node communication, enabling adaptation in non-stationary environments. The challenge of interference management has also been investigated through location-aware beamforming models that estimate interference effects based on user positioning [11]. In [12], a survey of new beamforming strategies tailored for MIMO and code-division multiple-access (CDMA) systems within 5G and beyond architectures was presented.

While these interference-aware methods are promising, they often rely on the availability of either explicit channel state information (CSI) or accurate channel models to operate effectively. However, acquiring and maintaining up-to-date CSI is known to be difficult with fast channel variations, high-dimensional antenna arrays, and hardware constraints [13], [14] among others. Moreover, the overhead associated with channel estimation and feedback can vanish the benefits of interference-aware optimization, especially in dynamic environments with mobility or blockage [15].

To alleviate the dependency of interference mitigation on accurate CSI, research has explored new solutions based on machine learning (ML), e.g., [16], [17]. Data-driven ML

arXiv:2602.22991v1 [eess.SP] 26 Feb 2026

models trained on measurement data or simulations, may infer useful channel-related information without explicitly relying on CSI. A comprehensive study [18] has highlighted their effectiveness in 5G networks.

Recently, digital twins (DTs), i.e., virtual replicas of physical systems, have gained attention as tool for simulating, optimizing, and controlling wireless networks in real time [19]–[22]. By creating virtual replicas of real-world assets, a DT provides an interactive and dynamic platform for analyzing performance, predicting behavior, and facilitating decision-making processes. In the context of communication networks, it is envisioned that DTs can improve network efficiency by a more efficient and accurate optimization of the main network parameters [23]. Due to the challenges of establishing and then maintaining directional links in a dynamic environment, beam management emerges as a suitable application for DT. In [24], the authors proposed a DT-assisted online interference-aware beam design framework to generate beam patterns that mitigate interference using only power measurements, without requiring explicit channel knowledge. The paradigm of leveraging limited measurements and data-driven optimization motivates also our research work.

Modern networks also include relays to extend coverage and improve reliability, especially in dense multi-user scenarios where interference becomes critical [25]. This issue is particularly acute in amplify-and-forward (AF) relay systems, where full CSI cannot be obtained for channels from and to the relay, as the relay does not measure signals but simply amplifies and forwards them, precluding direct channel estimation. By forwarding signals, relays may also increase a diversity gain and the overall system robustness. Relays may operate either in a decode-and-forward (DF) mode where the relay restores the received signal, or in an AF, made when the relay retransmit the received signal without decoding. While DF offers higher reliability, AF is simpler and more power-efficient [26].

Motivated by the limitations of existing literature, we study interference-unaware beamforming in a relay-assisted MIMO system WiFi scenario. Specifically, we propose an innovative framework, called prediction-assisted optimization (PAO), that learns the relay beamforming to maximize the signal-plus-interference-to-noise ratio (SINR) without requiring explicit CSI.

PAO operates in two stages. First, a neural network (NN) is trained in a supervised fashion to predict the positions of the target user and interfering transmitters based on power measurements. We denote this stage as the SINR-based localization (SL). The estimated positions are then used in a second stage where an optimization algorithm assisted by the DT determines the optimal relay beamforming configuration. We denote this step as Digital Twin-Assisted Optimization (DT-AO). The role of the DT is crucial since it is used to emulate the radio channel and evaluate candidate beam directions. To find the relay steering direction that maximizes the SINR at the access point (AP). This closed-loop approach reduces the need for physical CSI measurements across different relay beam configurations by leveraging predicted channel information from the DT. The NN model is trained and tested using both simulation data generated by a DT, and experimental

data obtained in realistic wireless conditions from a custom-built mmWave platform. This platform captures real-world effects that are difficult to reproduce in simulations, such as hardware imperfections, interference, and environmental variability, making our results more accurate and representative. Our simulations demonstrate that the proposed approach is robust to non-negligible localization errors. Notably, PAO achieves a near-optimal solution with around seven times less measurements than the benchmarks.

The remainder of this paper is organized as follows. Sec. II introduces the system model for the relay-assisted MIMO uplink in the presence of non-cooperative interferers. The proposed PAO framework is presented in Sec. III, describing its SL stage for position estimation and its DT-AO stage for relay beam refinement. Sec. IV details the design of the main system components, including the beamforming codebook, NN architecture, digital twin functions $f(\cdot)$ and $f'(\cdot)$, and the employed optimization algorithms, i.e. gradient-based optimization (GBO) and genetic algorithm (GA). Simulation and experimental results are reported in Sec. V, evaluating both localization accuracy and overall PAO performance. Finally, Sec. VI concludes the paper.

Notation: Throughout the paper, boldface capital letters and boldface lower-case letters such as \mathbf{X} and \mathbf{x} denote matrices and vectors, respectively. $(\cdot)^H$ denotes conjugate transpose. $\|\cdot\|$ and $|\cdot|$ represent the Frobenius norm and the cardinality of a set, respectively. $\mathbb{E}\{\cdot\}$ denotes the expectation operator.

II. SYSTEM MODEL

We consider a narrowband MIMO uplink transmission system, wherein the transmission from a station (STA) with a uniform planar array (UPA) of N_t antennas to a WiFi AP, also equipped with a UPA of N_r antennas, is assisted by an AF relay as shown in Fig. 1. In the vicinity of the AP, there are $K > 1$ non-cooperative devices, where device $k \in \{1, \dots, K\}$ has N_k antennas, operate at the same frequency bands and, therefore, causing interference.

We adopt a three-dimensional Cartesian coordinate system to describe the network geometry. Let

$$\mathbf{p}_0 = [x_0, y_0, z_0] \quad (1)$$

denote the position of the target STA, and

$$\mathbf{p}_k = [x_k, y_k, z_k], \quad k = 1, \dots, K, \quad (2)$$

denote the positions of the K non-cooperative interfering transmitters respectively. The positions of the AF relay and the AP are assumed to be fixed and known. The relative geometry between the STA, the interferers, the relay, and the AP determines the propagation paths associated with each link.

The AF relay includes two planar antenna arrays, with N_i and N_o antennas, to receive and transmit signals, respectively. The received signals are combined using a relay beamforming vector. The resulting complex scalar signal is then amplified and transmitted after applying a proper precoding beamformer. All channels, beamforming vectors, and signals are expressed in complex baseband equivalent form. The combining and

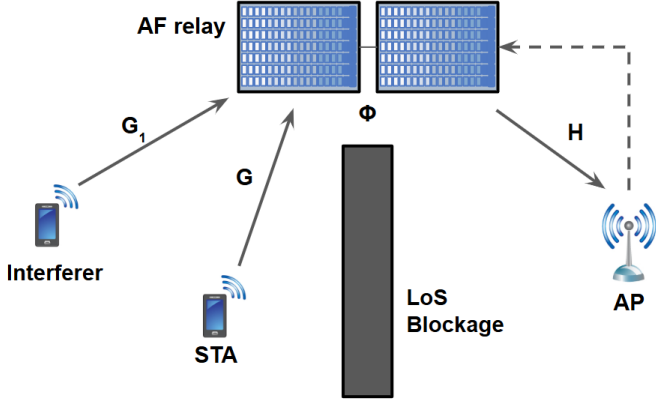


Fig. 1. System model. The direct link between the target STA to the Wifi AP is blocked, so transmission is assisted by an AF relay.

precoding vectors are designed to receive and transmit, respectively, signals from azimuth angles (θ_{Az}) and elevation angles (θ_{El}). Let us define angle vector $\theta = [\theta_{Az}, \theta_{El}]$, which contains the geometric propagation paths between the communicating nodes. Hence, to determine the angle-of-arrival (AoA) and angle-of-departure (AoD), as well as the corresponding channel responses, knowledge of the surrounding environment is required. In this work, the environment is assumed to be known and is used to characterize the propagation paths between nodes, enabling a geometry-based channel modeling. The beamforming vector $\mathbf{w}_N(\theta_{Az}, \theta_{El}) \in \mathbb{C}^{N \times 1}$, where $N = N_x N_y$, is obtained by vectorizing the $N_x \times N_y$ antenna array response:

$$[\mathbf{w}_N(\theta_{Az}, \theta_{El})]_n = e^{j \frac{2\pi}{\lambda} (d_x(n_x-1) \sin \theta_{El} \cos \theta_{Az} + d_y(n_y-1) \sin \theta_{El} \sin \theta_{Az})} \quad (3)$$

for $n = (n_y - 1)N_x + n_x$, with $n_x = 1, \dots, N_x$ and $n_y = 1, \dots, N_y$. Then, we denote the resulting phase control matrix of the AF relay (due to the combiner and precoder) as

$$\Phi(\theta_i, \theta_o) = A \mathbf{w}_{N_o}(\theta_o) \mathbf{w}_{N_i}^H(\theta_i), \quad (4)$$

where A is a fixed amplification coefficient. Matrix Φ identifies the *relay configuration*. We assume that the communication between the target STA and the AP only happens through the relay, while the line-of-sight (LoS) link is not available. We define $\mathbf{G} \in \mathbb{C}^{N_i \times N_t}$, $\mathbf{G}_k \in \mathbb{C}^{N_i \times N_k}$, and $\mathbf{H} \in \mathbb{C}^{N_r \times N_o}$ the channels between the STA and the relay, the k th interfering device and the relay, and the relay and the AP, respectively. The resulting cascaded channels from the target STA and the k th interferer to the AP are

$$\mathbf{C} = \mathbf{H} \Phi(\theta_i, \theta_o) \mathbf{G} \quad \text{and} \quad \mathbf{C}_k = \mathbf{H} \Phi(\theta_i, \theta_o) \mathbf{G}_k, \quad (5)$$

respectively. To model the received signal and emphasize the dependence on the unknown relay combining vector, we define the effective channel components as

$$\mathbf{h} = \mathbf{w}_{N_o}^H \mathbf{H} \mathbf{A} \mathbf{w}_{N_o}(\theta_o), \quad (6)$$

$$\mathbf{g} = \mathbf{G} \mathbf{w}_{N_t}(\theta_t), \quad \mathbf{g}_k = \mathbf{G}_k \mathbf{w}_{N_k}(\theta_k), \quad (7)$$

where $\mathbf{w}_{N_o}(\theta_o) \in \mathbb{C}^{N_o \times 1}$, $\mathbf{w}_{N_t}(\theta_t) \in \mathbb{C}^{N_t \times 1}$, and $\mathbf{w}_{N_k}(\theta_k)$ are the combining vector at the AP and the precoding vectors at the STA and K interference transmitters, respectively.

The relay-to-AP link is assumed fixed, with the relay precoder $\mathbf{w}_{N_o}(\theta_o)$ pointing directly toward \mathbf{p}_r and the AP combiner $\mathbf{w}_{N_i}(\theta_i)$ both are pointing directly toward \mathbf{p}_o pre-optimized under no interference on this link, and thus fixed. The AoA/AoD are derived from the relative 3D geometry. For a link from a transmitter at \mathbf{p}_A to a receiver at \mathbf{p}_B , the direction vector is

$$\Delta = \mathbf{p}_B - \mathbf{p}_A = [\Delta x, \Delta y, \Delta z]^T. \quad (8)$$

The corresponding spherical angles are

$$\theta_{El} = \arcsin\left(\frac{\Delta z}{|\Delta|}\right), \quad \theta_{Az} = \text{atan2}(\Delta y, \Delta x), \quad (9)$$

where $|\Delta| = \sqrt{\Delta x^2 + \Delta y^2 + \Delta z^2}$ is the Euclidean distance, $\arcsin(\cdot) \in [-\pi/2, \pi/2]$, and $\text{atan2}(\Delta y, \Delta x) \in [-\pi, \pi]$ gives the azimuthal angle in the xy -plane measured from the x -axis toward the y -axis. Furthermore, the STA UPA is assumed to be oriented toward the relay, so the STA precoding vector is optimized and fixed. However, the combining vector at the relay remains unknown and is to be designed.

Accordingly, as the STA transmits a symbol $x \in \mathbb{C}$ to the AP, and the other K interfering devices also transmit symbols $x_k \in \mathbb{C}$, $k = 1, \dots, K$, in the same time and frequency slot, the received signal at the AP can be expressed as

$$y = \mathbf{h} \mathbf{w}_{N_i}^H(\theta_i) \mathbf{g} x + \sum_{k=1}^K \mathbf{h} \mathbf{w}_{N_i}^H(\theta_i) \mathbf{g}_k x_k + n, \quad (10)$$

where $n \sim \mathcal{CN}(0, \sigma^2)$ is the additive white Gaussian noise (AWGN) with zero-mean and power σ^2 .

III. PREDICTION ASSISTED OPTIMIZATION FRAMEWORK FOR RELAY CONFIGURATION

In this section, we present the proposed PAO framework for relay configuration, which enables efficient beam optimization in interference-limited environments without requiring full CSI acquisition. As shown in Fig. 2, the framework integrates four main functional blocks: the Measurement Module, the Switching Control Unit, the SL Module, and the DT-AO component. These components jointly support localization-aware beam optimization and low-overhead communication. The overall operation alternates between a measurement phase and a communication phase, orchestrated by the Switching Control Unit in Fig. 2. During measurement, signal observations are collected and processed for environment inference, while during communication, the optimized relay configuration is applied for data transmission.

a) *Measurement Module*: As illustrated in Fig. 2, the Measurement Module is responsible for acquiring received signal power and interference-plus-noise power samples under different relay beam configurations. In measurement mode, a predefined codebook of beam directions is sequentially applied at the relay based on the signaling received from the AP through a control link, and the corresponding SINR values are computed directly from the measured powers without explicit channel estimation. This lightweight measurement process avoids the overhead of full CSI acquisition while still capturing the spatial and interference characteristics of the environment.

The resulting SINR observations are forwarded to the SL Module for further processing, as indicated in Fig. 2.

b) Switching Control Unit: The Switching Control Unit serves as the central coordinator of the framework, as depicted in Fig. 2. It dynamically switches the relay operation between measurement mode and communication mode based on control commands transmitted over a dedicated control link from the AP. In measurement mode, the Switching Control Unit activates the beam sweeping process and triggers the Measurement Module to collect SINR samples. Once sufficient measurements are obtained and an optimized configuration is identified, it transitions the relay to communication mode by applying the selected beam configuration to the RF chain. At the same time, it disables the measurement process and the DT-based optimization to minimize computational and signaling overhead, as shown in Fig. 2.

c) SL Module: The SL Module processes the measured SINR values provided by the Measurement Module in Fig. 2. It employs an NN to infer the spatial configuration of the environment, including the estimated positions of the target STA and interfering transmitters. By learning the mapping between beam-dependent SINR patterns and spatial layouts, the SL Module enables environment-aware decision making without explicit channel reconstruction. These predicted positions serve as inputs to the DT-AO component when further beam refinement is required, as illustrated in Fig. 2.

d) DT-AO: The DT-AO component leverages a DT as a virtual representation of the physical environment, as shown in Fig. 2. Using the position estimates provided by the SL Module, the DT emulates propagation conditions and interference effects to iteratively evaluate candidate relay beam configurations. Through simulated SINR feedback, the DT-AO component searches for a beam direction that maximizes link quality under the inferred environment conditions. Once a suitable configuration is found, the optimized beam parameters are sent to the Switching Control Unit, which applies them during communication mode as depicted in Fig. 2.

In this way, the DT is only engaged when optimization or reconfiguration is required, while regular communication relies solely on the selected relay configuration, resulting in a practical and resource-efficient architecture that tightly integrates learning, optimization, and hardware control.

A. Problem Formulation

We defined the received signal at the AP in (10). Based on this received signal model, and for notational simplicity, in the remainder of this section we denote the relay combining vector as $\mathbf{w}_{N_i}(\boldsymbol{\theta}_i) = \mathbf{w}(\boldsymbol{\theta})$. Under this notation, the resulting SINR at the AP can be expressed as

$$\gamma = \frac{|h \mathbf{w}^H(\boldsymbol{\theta}) \mathbf{g}|^2 P_x}{\sum_{k=1}^K |h \mathbf{w}^H(\boldsymbol{\theta}) \mathbf{g}_k|^2 P_{x_k} + \sigma^2}. \quad (11)$$

where P_x denotes the transmit power of the target STA, and P_{x_k} is the transmit power of the k th interfering signal.

The goal is configuring the relay to maximize the rate. From the received signal (11), the achievable channel rate between the target STA and the AP is

$$R = \log_2(1 + \gamma(\boldsymbol{\theta})), \quad (12)$$

Note that, since the relay precoding vector is fixed, optimization is performed solely over the relay combining vector. Since the combining vector is defined as a steering vector, its optimization comes down to finding the optimal azimuth and elevation angles, i.e., $\boldsymbol{\theta} = [\theta_{Az}, \theta_{El}]$, that maximize the SINR. Therefore, we aim at solving the following problem:

$$\hat{\boldsymbol{\theta}} = \arg \max_{\boldsymbol{\theta}} \gamma(\boldsymbol{\theta}). \quad (13)$$

In principle, this optimization can be easily performed with the assumption that full CSI is available. However, in practice, obtaining such information is challenging due to the large training overhead required for estimating multiple channel components, particularly in the presence of a relay [27]. The AF relay cannot measure the channel to the STA or to the AP, since it does not include a signal processing unit; thus such information can only be obtained by the AP through lengthy estimates at the cascade channel with several relay configurations. However, note that (11) depends solely on the power levels of the received and interference signals, and we will aim at maximizing γ using only power measurements. In particular, we measure the received STA power $|h \mathbf{w}(\boldsymbol{\theta}) \mathbf{g}|^2 P_x$, and the combined interference-plus-noise power $\sum_{k=1}^K |h \mathbf{w}(\boldsymbol{\theta}) \mathbf{g}_k|^2 P_{x_k} + \sigma$. Hence, we aim at optimizing the relay beam direction $\boldsymbol{\theta}$, using only these measured powers.

To this end, we propose a two-stage framework called PAO. In the first stage (SL, described in Sec. III-B), an NN is trained to estimate the positions of the STA and the interfering devices based on SINR measurements. The second step (DT-AO, described in Sec. III-C) optimizes the relay combining beam direction. This is accomplished through an iterative loop between a DT and an optimization algorithm, where the combining beam direction $\boldsymbol{\theta}$ is progressively refined using environmental insights provided by the DT. The process operates in a closed loop, continuously updating $\boldsymbol{\theta}$ to maximize γ . Figure 2 shows the overall scheme of the PAO framework. The use of DT enables to significantly reduce the number of CSI estimates (in the first stage) and still being able to infer the cascade channel for only relay configuration. This then enables computing the optimal configuration by explaining the digitally emulated environment.

B. SINR-based localization (SL)

The SL constitutes the first step of the proposed PAO framework, and aims at estimating the minimum-mean squared error (MMSE) positions of the target STA and interfering transmitters based on observed SINR measurements. We first define as the concatenation vector of the 3D coordinates of all $K + 1$ transmitters.

$$\mathbf{p} = [\mathbf{p}_0, \mathbf{p}_1, \dots, \mathbf{p}_K] \in \mathbb{R}^{3(K+1)} \quad (14)$$

the selection of the next candidate steering direction θ_{j+1} . We obtain a closed-loop procedure, where the optimization algorithm iteratively queries the DT with updated steering directions θ , and uses the returned SINR values $\hat{\gamma}$ to refine its search. The process continues until convergence (i.e., when no further improvement of the SINR is observed) or when a maximum number of iterations J is reached.

Remark: The optimization process is driven entirely by simulated feedback from the DT rather than using costly real-world measurements. By relying on the DT as a surrogate model for signal propagation and interference, the optimization algorithm can rapidly explore the steering direction space, and converge toward an SINR-optimal relay configuration requiring few interactions with the environment.

IV. DESIGN OF THE PAO FRAMEWORK COMPONENTS

In this section, we describe the design of the specific components of the proposed PAO framework introduced in Sec. III, which leverages position predictions to guide beam configuration decisions at the relay. In the next subsection IV-A we present the design of the configuration codebook \mathcal{C} used in the PAO SL step. This is followed by the description of the NN architecture employed for position prediction in IV-B. Next, in Sec. IV-C we introduce the functions $f(\cdot)$ and $f'(\cdot)$ that predict the received STAs powers of a candidate beam steering direction θ . Finally, in Sec. IV-D we explain the optimization algorithm that selects the beam direction maximizing the expected SINR according to the predicted positions.

A. Codebook Design

To construct codebook \mathcal{C} , we quantize the angular space into finite sets of azimuth and elevation angles, consisting of M elevation angles and N azimuth angles, based on the resolution limits imposed by the phase shifters. Specifically, we define the sets of quantized angles as $\Theta = \{\theta_1, \dots, \theta_M\}$, $\Xi = \{\xi_1, \dots, \xi_N\}$, where $\theta_{m+1} - \theta_m = \Delta_\theta$ and $\xi_{n+1} - \xi_n = \Delta_\xi$. The codebook \mathcal{C} is then constructed as the Cartesian product of these two angle sets, i.e.,

$$\mathcal{C} = \{(\theta_m, \xi_n)\}^{M \times N}. \quad (21)$$

Hence, the total number of codebook entries is $C = M \cdot N$.

B. Design of the NN

The NN is used in the PAO SL step to determine transmitter's and interferers' spatial positions. This is done by mapping a vector of measured SINRs to the spatial coordinates of the STA and interferers. The architecture of the NN includes L layers, each composed of B_ℓ neurons, $\ell \in \{1, \dots, L\}$, and is designed to learn the mapping from observed features to the predicted positions. Specifically, the $B_{\ell-1} \times 1$ vector \mathbf{F}_ℓ is the input of layer ℓ , where B_ℓ is the input dimension of layer ℓ . For the first layer ($\ell = 1$), we have $\mathbf{F}_1 = \bar{\Gamma}$, i.e., the vector of S SINR measurements. The output of the ℓ th hidden layer is calculated as $\mathbf{F}_{\ell+1} = g_\ell(\mathbf{W}_\ell \mathbf{F}_\ell + \mathbf{b}_\ell)$, where \mathbf{W}_ℓ (of size $B_\ell \times B_{\ell-1}$) and \mathbf{b}_ℓ (of size $B_\ell \times 1$) are the trainable weights and biases, respectively, and g_ℓ is the activation function for layer

ℓ . The output of the last layer ($\ell = L$) returns the vector of the predicted positions $\hat{\mathbf{p}} = g_L(\mathbf{W}_L \mathbf{F}_L + \mathbf{b}_L)$. The activation function in the last layer $g_L(\cdot)$ is typically chosen to fit the desired output properties. Since positions are continuous real values, a linear activation function is often used.

To improve generalization, the NN is first pre-trained on dataset \mathcal{D}_S , allowing it to learn a broad representation of the mapping from SINR to positions. The model is then refined on the dataset \mathcal{D}_T made of real SINR measurements to adapt to domain-specific characteristics. During refinement, some layers are frozen, keeping their weights fixed to retain previously learned representations, while the remaining layers are fine-tuned on \mathcal{D}_T .

Since we aim at minimizing the difference between he actual and predicted positions of the target STA and the interfering transmitters from we use the MSE loss function to train the NN, the training aims at minimizing, i.e.,

$$\text{MSE}(\bar{\mathbf{p}}, \hat{\mathbf{p}}) = \frac{1}{\|\mathcal{D}\|} \sum_{\bar{\mathbf{p}} \in \mathcal{D}} \|\hat{\mathbf{p}} - \bar{\mathbf{p}}\|^2, \quad (22)$$

where \mathcal{D} is either \mathcal{D}_S or \mathcal{D}_T according to the training phase.

C. Design of Functions $f(\cdot)$ and $f'(\cdot)$

The objective of the DT in the PAO DT-AO step is to simulate signal propagation and interactions in a realistic wireless environment. We employ MATLAB as a simulation engine for simplicity. First the digital beamformer is modeled using the phased array toolbox [28], multiple of these are then integrated into a site-viewer object which creates a 3D environment modeled after the real office used for the experimental measures. Finally, raytracing is also performed in MATLAB, using the communications toolbox. Using these tool we implemented the functions $f(\cdot)$ and $f'(\cdot)$. These functions take as inputs the estimated positions of the STA and interferers (vector \mathbf{p}) and a beam steering direction θ . The simulator constructs a complete transceiver system, including the antenna array geometry, scene layout, and channel characteristics. The function $f(\mathbf{p}, \theta)$ processes this geometry and steering direction to compute the received signal at the STA. In parallel, $f'(\hat{\mathbf{p}}_k, \theta_j)$ calculates the aggregate interference and noise power by summing contributions from interferers at positions $\hat{\mathbf{p}}_k$ under steering direction θ_j .

Remark: While a DT can be built using ray tracing to emulate the physical environment, this approach often is hard to implement. The complexity of tracing electromagnetic waves, combined with partial knowledge of material and simplified environmental models [29], limits the accuracy and scalability of ray-tracing-based DTs [30]. In contrast, data-driven surrogate models, such as NNs, can be trained directly on measured or simulated data, eliminating the need for detailed modeling of the environment [31]. This approach simplifies development but may be demanding in computational resources. Regardless of the method used to design the DT, the key advantage remains the same: the ability to optimize the precoding vector effectively with significantly fewer real-world interactions, providing a more efficient and cost-effective alternative to traditional approaches based on

real measurements. In this work, a ray-tracing-based DT is adopted due to environment information availability and its relatively lower computational cost compared to large-scale data-driven training pipelines, making it a practical and reproducible choice for the considered scenario.

D. Design of the Optimization Algorithm

To find the optimal beam steering direction θ in the PAO DT-AO step by (13), we consider two optimization algorithms: the GBO algorithm and the GA.

Gradient-Based Optimization (GBO): This method employs a multi-start interior-point algorithm initialized from multiple starting points, denoted by D_{MS} , which correspond to different initial beam steering directions $\theta \in \{\theta_1, \theta_2, \dots, \theta_{D_{MS}}\}$. These directions are considered to thoroughly explore the solution space and mitigate the risk of converging to poor local minima. For each initial steering direction θ_d , with $d = 1, \dots, D_{MS}$, the constrained nonlinear multivariable function is maximized, resulting in a local maximum $\hat{\theta}_d$. Since multiple initial points can lead to the same local maximum, the set of the obtained unique local maximum is denoted by $\mathcal{M} = \{\hat{\theta}^{(1)}, \hat{\theta}^{(2)}, \dots, \hat{\theta}^{(K)}\}$, $K \leq D_{MS}$.

Among the K unique local minima in \mathcal{M} , the solution of (13) is obtained as

$$\hat{\theta}_{\text{GBO}} = \arg \max_{\hat{\theta} \in \mathcal{M}} \hat{\gamma}(\hat{\theta}). \quad (23)$$

Genetic Algorithm (GA): The GA is an optimization method that is well-suited for highly nonconvex and multimodal optimization problems. It is based on the principle of natural selection, where a population of candidate solutions evolves over successive generations. Specifically, at each generation g , the population consists of G individuals θ_g , $g = 1, \dots, G$, where θ_g represents a candidate beam steering direction. The fitness of each individual is evaluated based on the objective function, where a higher SINR corresponds to better fitness. Through selection, crossover, and mutation operations, the population gradually evolves towards high-performing solutions. Upon convergence, the individual yielding the best fitness is selected as the final output, that is

$$\hat{\theta}_{\text{GA}} = \arg \max_{\{\hat{\theta}_g, g=1, \dots, G\}} \hat{\gamma}(\hat{\theta}_g), \quad (24)$$

where G is the index of the final generation. Through these evolutionary steps, the population is iteratively updated to promote the emergence of beam steering directions that effectively solve (13).

V. NUMERICAL RESULTS

In this section, we evaluate and discuss the performance of the proposed PAO framework for the optimization of the relay configuration.

A. Experimental Setup

Our proposed PAO framework is trained and validated using both simulated and experimental data. Specifically, we compute and collect the received signal strength indicator

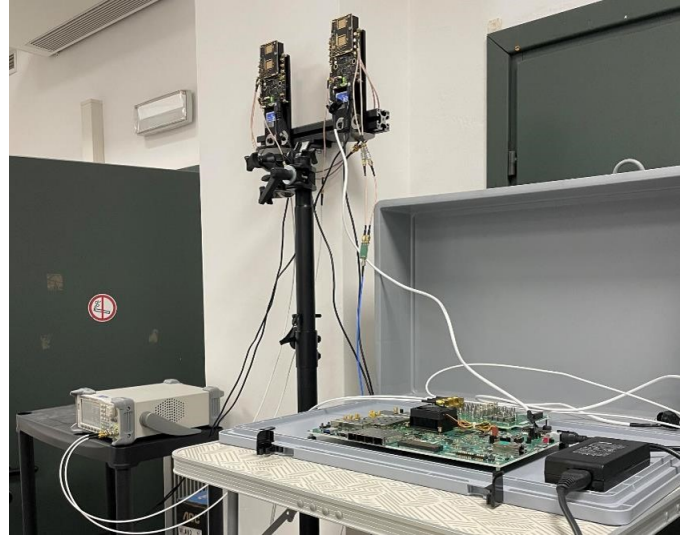


Fig. 3. Photograph of the mmWave relay prototype composed of two Siviers EVK06003 beamforming modules, integrating 16-element antennas and RF front-end functionalities for transmission and reception in the 60 GHz band.

(RSSI) as a reference power measurement, for different beam steering directions, to then compute the SINR.

The RF mmWave front-ends consist of Siviers EVK06003 [32] modules, which integrate beamforming and up/down conversion functionalities using a 16-element URA antenna in a 2×8 configuration. The beamformers operate with a predefined codebook that covers a grid of directions with azimuth angles ranging from -54° to $+54^\circ$ in 5.4° steps, and elevation angles of $+18^\circ$, 0° , and -18° . The devices support frequency conversion between 59 and 67 GHz; for the experiments, we operate in the ISM band at a central frequency 60.48 GHz, as illustrated in Fig. 3.

Baseband signal generation and acquisition are handled by an RFSoc ZCU111 platform [33], which interfaces with both the STA and the AF relay receiver. The interfering transmitter is implemented using a pre-programmed ADALM-Pluto SDR.

Both the STA and interfering transmitters are configured to use their optimal beam steering directions, and the alignment with the receiver is achieved using a laser for precise pointing. This alignment simplifies the dataset by reducing beam misalignment variability. As shown in Fig. 4, power measurements are collected at the AF relay receiver from 30 distinct positions of the target transmitter, with 20 beam steering direction sweeps per position. Positions are labeled from A1 to A15 and from B1 to B15, and arranged along two parallel lines (A and B) corresponding to the longer sides of a $1.5\text{m} \times 1\text{m}$ rectangle in the x - y plane.

B. Simulation Setup

For the simulations, we use a custom MATLAB-based DT simulator, so as it can be properly integrated with a MATLAB ray-tracing simulation engine to model realistic signal propagation within the environment. The tracer simulates up to two reflections, the carrier frequency and antenna configurations are those of Sec. V-A. The nodes are deployed in a reconstructed indoor environment with the same structure,

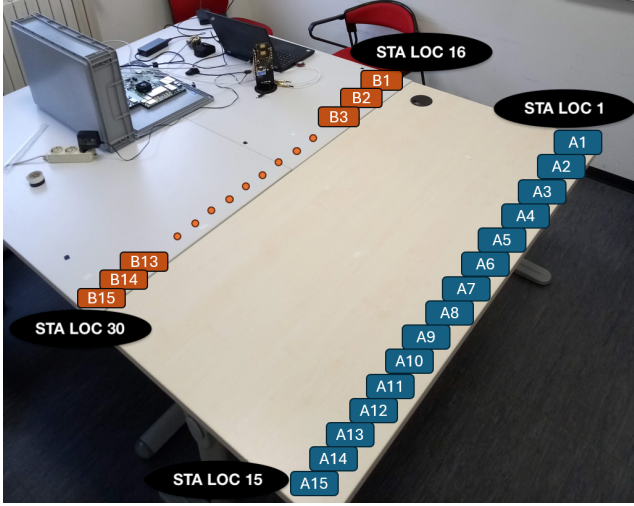


Fig. 4. The transmitter array consists of 30 positions, organized into two parallel rows along the longer sides of a 1.5 m \times 1 m rectangle in the x - y plane. Each row contains 15 positions, evenly spaced at 0.1 m. Positions A and B denote the first and last transmitter locations along each row.

TABLE I
SIMULATION PARAMETERS.

Parameter	Description	Value
F_0	Operating frequency	60.48 GHz
λ	Wavelength	c/F_0
B	Bandwidth	1.2×10^9 Hz
N_t, N_i, N_o, N_r, N_k	Antenna array structure	2×8
T_{xloc}	Transmitter xyz position	$[x_{tx}, y_{tx}, 0.9]$
R_{xloc}	Receiver xyz position	$[9, 2, 1.2]$
AF_{Rxloc}	AF receiver relay xyz position	$[7, 5.5, 2]$
AF_{Txloc}	AF transmitter relay xyz position	$[7.2, 5.5, 2]$
I_{loc}	Interferer position	$[x_{int}, y_{int}, 0.9]$
x_{min}, x_{max}	Min-max range for x	3.4 - 6.5 m
y_{min}, y_{max}	Min-max range for y	1 - 2.9 m
x_{tx}, y_{tx}	Transmitter coordinates	$\in [x_{min}, x_{max}] \times [y_{min}, y_{max}]$
x_{int}, y_{int}	Interferer coordinates	$\in [x_{min}, x_{max}] \times [y_{min}, y_{max}]$
P_{Tx}	Transmitter power	0.1 W
P_i	Interferer power	0.1 W
Θ	Azimuth angle	$\in [-54^\circ, 54^\circ]$
Ξ	Elevation angle	$\{-18, 0, 18\}$

and spatial layout as in the experiments, as illustrated in Fig. 5, where all relevant environmental elements are reproduced to ensure high fidelity between simulated and experimental scenarios. In particular, the 3D DT includes the structural components of the environment as well as the objects present in the setup, and accurately represents the placement and disposition of the AF relay, transmitters, and receivers according to the experimental configuration. The simulation parameters are reported in Table I.

To generate training and testing samples, the transmitter and interferers are randomly placed within the x - and y -boundaries of the room, defined by x_{min} , x_{max} , y_{min} , and y_{max} . To maintain consistency with the experimental campaign and avoid unrealistic deployments (e.g., nodes positioned under the furniture), the z -coordinate of the nodes is fixed. The beamforming codebook in the DT simulator is also obtained from

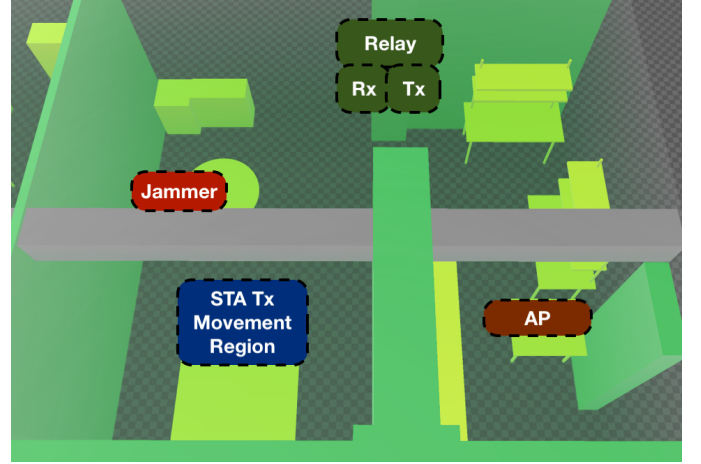


Fig. 5. Recreated 3D DT of the experimental environment employed for simulations, reproducing all structural and spatial features. The model incorporates walls, doors, windows, furniture, and other relevant elements of the setup. Furthermore, the spatial disposition of the AF relay, transmitters, and receivers is modeled according to the experimental configuration.

the experimental hardware via reverse calibration. Specifically, the beam steering directions at 0° azimuth and 0° elevation, ideally identical in theory, are used as reference calibration values. Then, we normalize all other beam steering directions in the codebook with respect to this reference to reproduce beam patterns in the DT simulator that accurately reflect the actual hardware behavior, and ensuring consistency with the experimental setup.

Figure 6 compares the received signal power at the AP measured in the experimental setup with that obtained from the simulated setup across different beam steering directions. A noticeable similarity in the observed patterns is found between the two, supporting the use of a DT to emulate realistic wireless scenarios. The performance of the proposed PAO beamforming framework depends on how accurately the DT represents the actual environment, which is supported by this step.

C. SL Performance

In this section we evaluate the performance of the SL step, and measure the root mean square error (RMSE) of the transmitter's and interferers' predicted positions and the SINR. The PAO framework consists of two steps, namely SL and DT-AO. Actually, the performance of DT-AO relies on the transmitter's and interferers' positions predicted by the NN in the SL step. For this reason, we start the evaluation by focusing on the prediction performance of SL, measured in terms of the RMSE of the predicted positions, and the resulting effect on the SINR. To train the NN, we first generate a synthetic dataset \mathcal{D}_S consisting of 10,000 simulated samples using a DT as described in Sec. V-B. Each sample includes the positions of the transmitter and an interferer, along with the corresponding SINR values under multiple beam configurations. This dataset is used to pre-train the model. For fine-tuning, we use real-world laboratory data denoted as \mathcal{D}_T , which comprises 600 samples collected across 30 distinct locations as described in

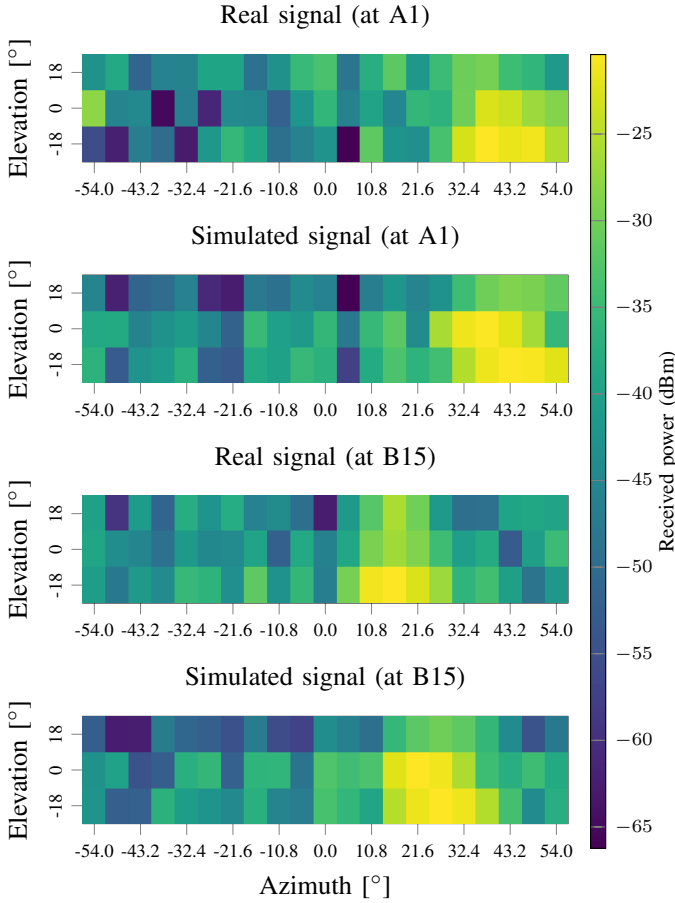


Fig. 6. Comparison between simulated and experimental receive power for transmitter positions A1 and B15 (see Fig. 4). The receive power is shown for each receiving beam. Simulated results are obtained using a ray-tracing propagation model with up to two reflections.

Sec. V-A, with 20 repeated measurements per location under consistent environmental conditions. During this stage, we freeze the early layers of the NN, and only update the deeper, more task-specific layers. Fine-tuning is carried out for a small number of epochs using a reduced learning rate, allowing the model to adapt to real-world conditions while retaining the knowledge acquired from the synthetic data. We consider $S \in \{3, 5, 7, 11, 21, 63\}$ possible beam directions, to evaluate the trade-off between codebook resolution and accuracy. Then, the RMSE is computed as

$$\text{RMSE}(\bar{\mathbf{p}}, \hat{\mathbf{p}}) = \sqrt{\frac{1}{\|\mathcal{D}_T\|} \sum_{\bar{\mathbf{p}} \in \mathcal{D}_T} \|\hat{\mathbf{p}} - \bar{\mathbf{p}}\|^2}, \quad (25)$$

where $\bar{\mathbf{p}}$ and $\hat{\mathbf{p}}$ are the ground-truth and predicted positions, respectively. We adopt a leave-one-location-out refinement strategy: at each iteration, data from 29 locations are used for fine-tuning, while the remaining location is used for the testing. This process is repeated for all 30 locations to ensure generalization.

Figure 7 shows the RMSE of the predicted positions as a function of the input codebook dimension S , which corresponds to the number of real SINR measurements used as

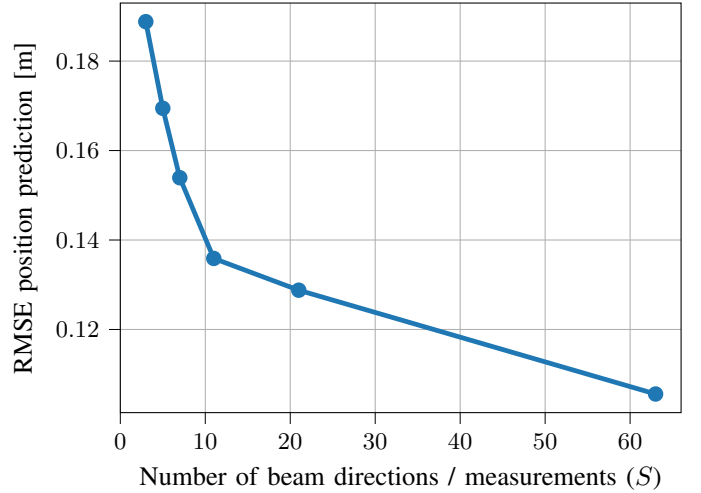


Fig. 7. RMSE of the predicted positions as a function of the input dimension S . Each point corresponds to a independently trained NN.

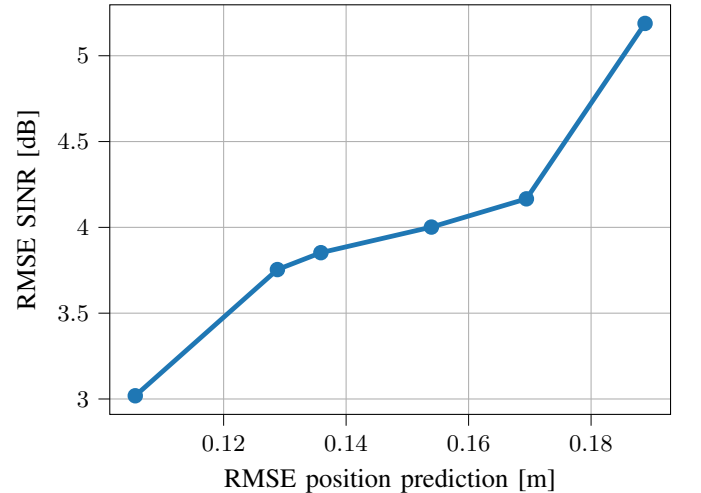


Fig. 8. RMSE of the predicted SINR (relative to the true SINR) vs. the RMSE of the predicted positions (relative to the true positions).

input to the NN model. Each point in the curve represents a separately trained NN. Notably, beam steering directions are selected by initially fixing the elevation angle to 0° and uniformly scanning the azimuth space. As S increases, additional measurements are taken at higher elevation angles, thereby providing more spatially diverse input features. The results show that increasing S significantly improves localization accuracy. Specifically, the RMSE decreases steeply up to $S = 11$. Then, for $S > 11$, the performance gain becomes marginal, suggesting that using $S^* = 11$ beam steering directions provides a good balance between prediction accuracy and the effort required to collect measurements.

Figure 8 shows the RMSE of the predicted SINR, computed as the difference between the SINR at the predicted positions and the SINR at the actual positions, plotted against the RMSE of the predicted positions. As expected, the RMSE SINR increases with the position error, meaning that improved

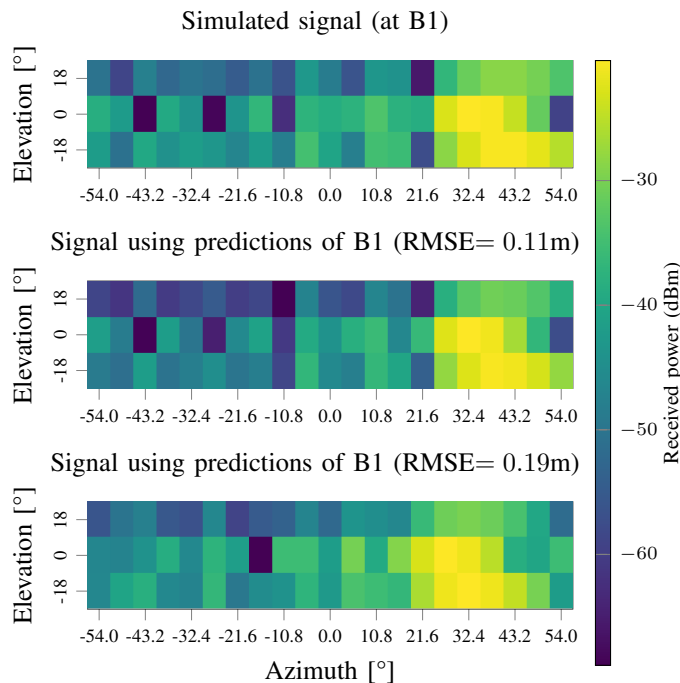


Fig. 9. Received power per beam at position B1. We use the true positions (top) and the predicted positions from experimental data using an NN. Prediction errors are expressed in terms of the RMSE.

position prediction accuracy translates into more accurate SINR estimation. This is consistent with (20), where the SINR is modeled as a spatially-dependent function. Notice that the trend in Fig. 8 closely resembles that in Fig. 7.

In addition, Fig. 9 reports the receive power per beam at position B1 (see Fig. 4). The signal strength is measured either relative to the true positions of the transmitter, or the predicted positions from the NN. The results show that, as the position error (expressed in terms of the RMSE) increases, the mismatch between the true and NN-predicted receive power also increases. Nevertheless, despite the moderate positioning error, the spatial structure of the received power is preserved in both cases, with minor network performance degradation.

D. PAO Convergence Efficiency Demonstration

For the simulator, we use a ray-tracing propagation model with up to two reflections. First, in Fig. 10 we compare the performance of the proposed PAO framework with a classical linear grid interpolation-based approach, which operates on measurements obtained from a predefined codebook of relay configurations. These measurements start with an initial codebook configuration, followed by incrementally activating neighboring configurations in the grid, each requiring a new measurement by the relay, enabling gradual linear interpolation across the measured SINR values to estimate continuous positions, in terms of the SINR obtained with the best AF relay steering direction. Notice that the interpolation method operates directly on ground-truth positions obtained from the simulations, and therefore does not rely on learning models; so, it serves as a heuristic optimization benchmark for PAO.

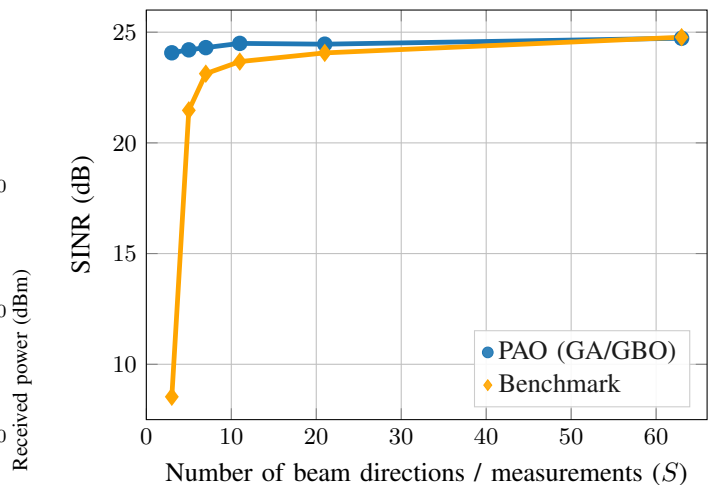


Fig. 10. SINR of the proposed PAO framework vs. an interpolation-based benchmark using acquired data, as a function of the input dimension S (i.e., the number of real beam measurements used per sample).

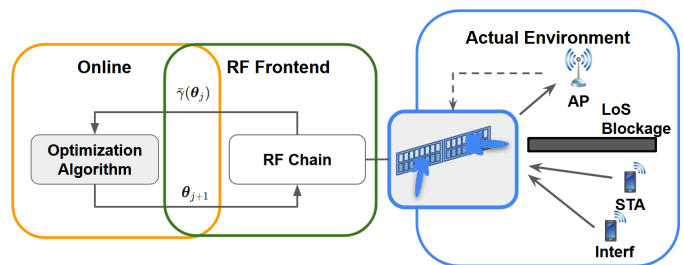


Fig. 11. Baseline workflow: direct application of GA/GBO to the real setup, requiring dense measurements at each optimization step.

In contrast, PAO operating with experimental data, is source of a prediction error compared to the interpolation approach.

The results show that PAO converges to a better solution significantly faster, and requires fewer measurements to determine an optimal AF relay configuration. Eventually, it returns a higher SINR. This improvement is attributed to the fact that PAO uses a DT simulator that emulates the wireless environment, enabling beamforming optimization without relying on dense experimental data. In contrast, the interpolation method only depends on ground-truth positions, and requires more data to achieve comparable performance.

E. Optimization Workflow Efficiency

Ideally, the baseline would rely entirely on real-world power measurements acquired with the experimental setup described in Sec. V-A. However, the experimental dataset \mathcal{D}_T contains only a limited number of samples. To increase the number of samples, we also consider synthetic data generated by the emulated environment in the DT, which has previously demonstrated high fidelity in reproducing real-world behavior (see Fig. 6). In this context, the beamforming angles θ_{Az} and θ_{El} are optimized over a continuous search space $[0, \pi]$, which cannot be directly supported by the hardware implementation based on a quantized codebook.

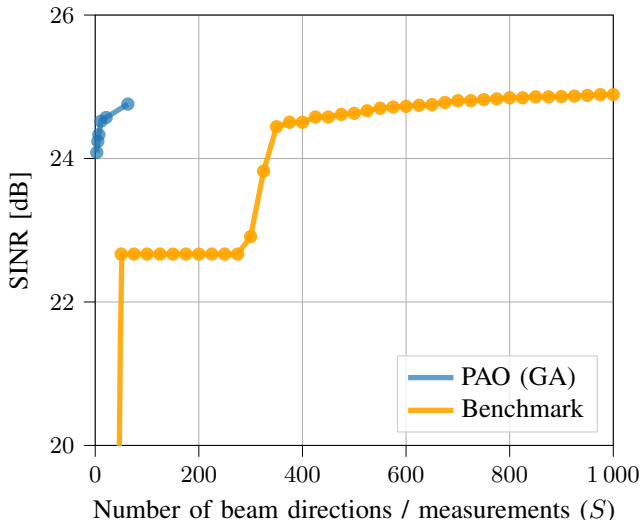


Fig. 12. SINR of the proposed PAO framework with GA optimization, vs. a benchmark using only real data, as a function of the input dimension S (i.e., the number of real beam measurements per sample).

As shown in Fig. 11, the baseline applies GA or GBO directly to the real setup, which requires extensive measurements from the environment at every optimization step. In contrast, PAO (see Fig. 2) does not apply the optimization algorithms directly on the real hardware. Instead, PAO first predicts the channel conditions and user positions using the DT, and then performs most of the GA or GBO optimization within this simulated environment. Only a limited number of real-world measurements are required to further refine these predictions.

In Figure 12 we plot the SINR using PAO with GA optimization. We see that PAO achieves relatively high SINR values after only a limited number of real-world measurements ($S < 63$). This efficiency is due to the fact that most of the optimization is performed within the DT simulator, reducing the need for costly measurements. The orange line represents the baseline without PAO, which typically requires significantly more measurements, and still provides negligible SINR improvements. We observe an initial sharp increase of the SINR, followed by more gradual improvements as additional measurements are considered. This trend reflects the typical behavior of GA-based optimization, where the algorithm first explores a wide range of possible solutions (exploration), and then gradually refines the best candidates (exploitation), resulting in slower but consistent improvements as it converges toward an optimal beamforming configuration.

Then, in Fig. 13 we consider PAO with GBO optimization, for $D_{MS} \in \{25, 50, 75, 100\}$. Each value of D_{MS} indicates the number of random starting points used in the optimizations. As a benchmark, instead of using the full PAO framework, we use only the GBO algorithm applied directly to the actual environment. Unlike with GA, we now observe multiple, smaller, abrupt jumps in the SINR, particularly as D_{MS} increases. This behavior arises because the GBO algorithm evaluates several candidate solutions simultaneously and selects the best-performing one at each iteration, resulting in sudden improvements whenever a superior solution is discov-

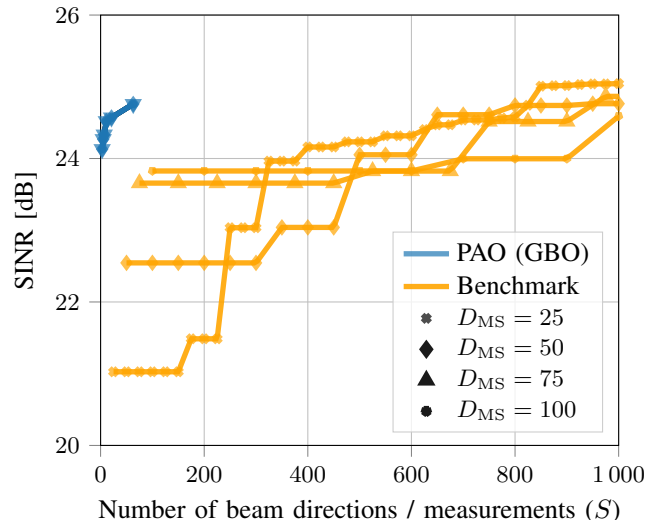


Fig. 13. SINR of the proposed PAO framework with GBO optimization as a function of D_{MS} , vs. a benchmark using only real data, as a function of the input dimension S (i.e., the number of real beam measurements per sample).

ered among the parallel runs. From these results, two distinct optimization behaviors emerge. The GA method undergoes an initial exploratory phase with notable SINR improvements, followed by a phase of gradual and continuous refinement as it converges toward an optimal beamforming solution. On the other hand, the GBO method produces a more irregular progression, characterized by moderate performance jumps corresponding to the selection of the best candidate from multiple parallel optimization paths. Increasing the number of multistarts D_{MS} amplifies this effect by increasing the probability of finding better initial solutions early in the optimization process.

VI. CONCLUSIONS

In this paper, we proposed a novel PAO framework for beamforming design in AF relay-assisted MIMO systems. Our proposed method operates in two stages. The first stage leverages a NN trained to predict the locations of both target and interfering transmitters solely from received power measurements, neglecting the need for explicit CSI. The second stage employs a DT-assisted optimization algorithm that iteratively refines the relay's beamforming direction using the predicted device positions to maximize the SINR at the intended receiver. Simulation results demonstrate the effectiveness of the proposed approach in balancing the trade-off between transmitter position prediction accuracy and beamforming performance. Furthermore, integrating the DT significantly reduces the need of real-world measurements, while maintaining robust interference mitigation even under localization uncertainties. Therefore, the PAO framework can be seen as a promising solution for dynamic and interference-rich wireless environments.

REFERENCES

- [1] A. Alkhateeb, J. Mo, N. Gonzalez-Prelcic, and R. W. Heath Jr., "MIMO precoding and combining solutions for millimeter-wave systems," *IEEE Commun. Mag.*, vol. 52, no. 12, pp. 122–131, Dec. 2014.

- [2] C. N. Barati, S. A. Hosseini, M. Mezzavilla, S. Rangan, and S. Vishwanath, "Directional cell discovery in millimeter wave cellular networks," *IEEE Trans. Wirel. Commun.*, vol. 14, no. 12, pp. 6664–6678, Dec. 2015.
- [3] M. Giordani, M. Mezzavilla, and M. Zorzi, "Initial access in 5G mmWave cellular networks," *IEEE Commun. Mag.*, vol. 54, no. 11, pp. 40–47, Nov. 2016.
- [4] IEEE, "IEEE Standard for Information technology–Telecommunications and information exchange between systems–Local and metropolitan area networks–Specific requirements–Part 11: Wireless LAN Medium Access Control (MAC) and Physical Layer (PHY) Specifications–Amendment 3: Enhancements for Very High Throughput in the 60 GHz Band," IEEE Standard 802.11ad-2012, 2012.
- [5] 3GPP, "Study on new radio access technology physical layer aspects," *TR 38.802*, 2017.
- [6] Q. Li, M. Ghogho, and H. Huang, "Interference-aware codebook design and beam selection for millimeter-wave systems," *IEEE Communications Letters*, vol. 23, no. 7, pp. 1177–1180, May 2019.
- [7] Y. Zhu and J. Wang, "Interference analysis and suppression in dense millimeter wave communication systems," *IEEE Trans. Wirel. Commun.*, vol. 15, no. 10, pp. 6515–6527, 2016.
- [8] M. Costa, "Writing on dirty paper," *IEEE Trans. Inf. Theory*, vol. 29, no. 3, pp. 439–441, 1983.
- [9] V. R. Cadambe and S. A. Jafar, "Interference alignment and degrees of freedom of the K-user interference channel," *IEEE Trans. Inf. Theory*, vol. 54, no. 8, pp. 3425–3441, 2008.
- [10] Y. Zhang and A. Alkhateeb, "Decentralized Interference-Aware Codebook Learning in Millimeter Wave MIMO Systems," *IEEE Trans. Commun.*, vol. 73, no. 5, pp. 3608–3621, 2025.
- [11] W. Liu, M. Chen, and J. Wang, "A Model for Interference Evaluation in 5G mmWave Ultra-Dense Networks Using Location-Aware Beamforming," *Information*, vol. 14, no. 1, p. 40, 2023.
- [12] H. Singh, R. Verma, and M. Kaur, "Interference Mitigation in B5G Network Architecture for MIMO and CDMA Systems: State of the Art and Challenges," *Information*, vol. 15, no. 12, p. 771, 2024.
- [13] J. Choi, V. Va, N. Gonzalez-Prelcic, and R. W. Heath Jr., "Millimeter-wave vehicular communication to support massive automotive sensing," *IEEE Communications Magazine*, vol. 54, no. 12, pp. 160–167, Dec. 2016.
- [14] A. Alkhateeb, G. Leus, and R. W. Heath Jr., "Compressed sensing based multi-user millimeter wave systems: How many measurements are needed?" in *Proc. IEEE International Conference on Acoustics, Speech and Signal Processing (ICASSP)*, 2015.
- [15] F. Carpi, S. Venkatesan, J. Du, H. Viswanathan, S. Garg, and E. Erkip, "Precoding-oriented Massive MIMO CSI Feedback Design," in *Proc. IEEE International Conference on Communications*, 2023.
- [16] H. Huang, Y. Song, J. Yang, G. Gui, and F. Adachi, "Deep-learning-based millimeter-wave massive MIMO for hybrid precoding," *IEEE Trans. Veh. Technol.*, vol. 68, no. 3, pp. 3027–3032, 2019.
- [17] H. Huang, J. Yang, H. Huang, Y. Song, and G. Gui, "Deep learning for super-resolution channel estimation and DOA estimation based on array signal processing," *IEEE Trans. Veh. Technol.*, vol. 67, no. 9, pp. 8549–8560, 2018.
- [18] N. Trabelsi, L. Chaari Fourati, and C. S. Chen, "Interference management in 5g and beyond networks: A comprehensive survey," *Computer Networks*, vol. 239, p. 110159, 2024. [Online]. Available: <https://www.sciencedirect.com/science/article/pii/S1389128623006047>
- [19] Z. Zhang, Z. Peng, H. Yu, M. Chen, and Y. Liu, "Digital network twins for next-generation wireless: Creation, optimization, and challenges," *IEEE Network*, pp. 1–9, 2025.
- [20] A. Shamsoshoara, R. Jurdak, A. Dorri, S. Gharib, and M. Mahmoudi, "A survey on digital twin: Definitions, characteristics, applications, and future research directions," *IEEE Internet of Things Journal*, vol. 11, no. 3, pp. 3903–3920, 2024.
- [21] N. Paglierani, F. Linsalata, O. A. Sevimay, L. Cazzella, D. Badini, M. Magarini, and U. Spagnolini, "Digital network twin-enabled synchronization and localization," *IEEE Journal on Selected Areas in Communications*, pp. 1–1, 2025.
- [22] R. Pegurri, D. Gasco, F. Linsalata, M. Rapelli, E. Moro, F. Raviglione, and C. Casetti, "Van3twin: the multi-technology v2x digital twin with ray-tracing in the loop," *arXiv preprint arXiv:2505.14184*, 2025.
- [23] D. Vasisht, R. Sharma, and A. Kumar, "Digital twin assisted framework for interference nulling in wireless networks," *arXiv preprint arXiv:2301.13311*, 2023.
- [24] Y. Zhang, T. Osman, and A. Alkhateeb, "A digital twin assisted framework for interference nulling in millimeter wave mimo systems," in *Proc. IEEE International Conference on Communications Workshops (ICC Workshops)*, 2023, pp. 248–253.
- [25] R. Chataut and R. Akl, "Massive MIMO Systems for 5G and beyond Networks—Overview, Recent Trends, Challenges, and Future Research Direction," *Sensors*, vol. 20, no. 10, 2020.
- [26] M. Pagin, M. Giordani, A. A. Gargari, A. Rech, F. Moretto, S. Tomasin, J. Gambini, and M. Zorzi, "End-to-end simulation of 5G networks assisted by IRS and AF relays," in *Proc. IEEE 20th Mediterranean Communication and Computer Networking Conference (MedComNet)*, 2022.
- [27] H. Kaur, M. Khosla, and R. K. Sarin, "Channel estimation in a mimo relay system: Challenges and approaches channel estimation in mimo relay system: A review," in *International Conference on Inventive Systems and Control (ICISC)*, 2018.
- [28] MathWorks, "Phased Array System Toolbox," 2025, accessed: 2025-09-29. [Online]. Available: <https://www.mathworks.com/products/phased-array.html>
- [29] M. Lecci, P. Testolina, M. Polese, M. Giordani, and M. Zorzi, "Accuracy versus complexity for mmWave ray-tracing: A full stack perspective," *IEEE Trans. Wirel. Commun.*, vol. 20, no. 12, pp. 7826–7841, Dec. 2021.
- [30] M. Ying, D. Shakya, P. Ma, G. Qian, and T. S. Rappaport, "Site-Specific Location Calibration and Validation of Ray-Tracing Simulator NYURay at Upper Mid-Band Frequencies," *arXiv preprint arXiv:2507.22027*, 2025.
- [31] Á. Bárkányi, T. Chován, S. Németh, and J. Abonyi, "Modelling for Digital Twins—Potential Role of Surrogate Models," *Processes*, vol. 9, no. 3, 2021.
- [32] S. Semiconductors. Rf module evk06003. [Online]. Available: <https://www.sivers-semiconductors.com/sivers-wireless/wireless-products/evaluation-kits/>
- [33] *ZCU111 Evaluation Board User Guide*, Xilinx, 10 2022, rev. 1.3.